International Conference on Space Optics—ICSO 2022

Dubrovnik, Croatia

3–7 October 2022

Edited by Kyriaki Minoglou, Nikos Karafolas, and Bruno Cugny,

Spectral and spatial filtering for daytime deep-space optical communications

Spectral and spatial filtering for daytime deep-space optical communications

Szymon Gladysz [a], Raphael Bellossi [a], Andreas Zepp [a], Douglas McDonald [a], Max Segel [a], Ruth Mackey [b], Niamh Fitzgerald [b], Karin Stein [a]

[a] Fraunhofer IOSB, Ettlingen, Fraunhofer Institute of Optronics, System Technologies and Image Exploitation, Gutleuthausstr. 1, 76275 Ettlingen, Germany; [b] mBryonics Ltd, Galway, Ireland

ABSTRACT

In deep-space optical communications, one particular challenge encountered at the ground receiver side are the wavefront deformations caused by atmospheric turbulence. This gives rise to reduced signal-to-background ratios and signal fades, especially during daytime. Background rejection is therefore a fundamental requirement for optical links operating in the low-photon-count regime with a strong solar background. Both, spectral and spatial filtering subsystems are essential for this application. To this end, we have analyzed several spectral filters and wavefront sensing approaches. In laboratory experiments, a combination of a bandpass filter and a Fabry-Pérot etalon delivered the required bandwidth of 0.17 nm and transmission of 90%, while a SWIR Shack-Hartmann sensor, combined with custom-built wavefront reconstruction software, directed the adaptive optics loop. We have obtained improvements in the Strehl ratio for signal-to-background ratios down to 0.2

Keywords: adaptive optics, wavefront sensing, transmission filters, atmospheric turbulence, deep-space optical communications

1. INTRODUCTION

The European Space Agency prepares technologies necessary for the implementation of future deep-space optical communications capabilities. One particular mission scenario involves a satellite in Mars orbit transmitting data modulated on a 1550 nm laser to a ground station. According to preliminary simulations, this optical downlink will work well during night-time but diffuse solar radiation and strong, ground-level turbulence will severely limit the link's effectiveness in daytime conditions. The Signal-to-Background Ratio (SBR) will be particularly small when the satellite is positioned angularly close to the Sun when observed from the Earth's surface.

Low SBR values are exacerbated by optical wavefront deformations caused by atmospheric turbulence. These wavefront deformations can lead to significant spatial spreading of the laser spot on the communications detector. If these effects cannot be mitigated then the ground terminal must be equipped with a detector that admits a larger angular field of view on the sky than otherwise required, and thereby admits a greater fraction of any sky background radiation (e.g. scattered sunlight). This, in turn, can dramatically lower the SBR and translate to increase in the bit-error rate.

Background rejection is therefore a fundamental requirement for optical links operating in the low-photon-count regime during the day[1]. Both, spectral filtering by an ultra-narrow-band optical transmission filter, as well as spatial filtering by an adaptive optics (AO) system to minimize the spot size of the downlink beam, are essential for this application. Fraunhofer IOSB and mBryonics have been commissioned with the task of designing spatial and spectral background filtering subsystems of the "Highly Selective Filter System" demonstrator.

The simulations which have led to the choice of the Shack-Hartmann sensor (SHS) in AO as well as prediction of achievable data rates in hypothetical systems operating on telescopes with apertures between 1 and 6 m can be found in the companion paper[2]. In this paper we focus on: the analysis of spectral filtering technologies suitable for deep-space communications during the day, characterization of the filters chosen in this project, as well as a description of the laboratory AO demonstrator and the results obtained with it. We also present a roadmap to an operational system.

2. ULTRA-NARROW-BAND TRANSMISSION FILTERS

A narrow-band filter transmits incident radiation in one spectral region while rejecting the wider spectral band. This is typically accomplished by using constructive and destructive interference in thin films. A spectral optical filter is designed for a central wavelength λ_C, at which the filter provides the maximum transmission efficiency. This efficiency decreases with deviation from λ_C. The filter bandwidth is defined by the wavelength range over which the filter power transmission efficiency is greater than 50% of its peak value. This bandwidth corresponds to the ability of the filter to block out-of-band radiation. For a spectral filter, this bandwidth should be as narrow as possible, especially in the case of photon-starved optical systems such as those used in deep-space optical communications. As the Doppler effect can shift λ_C by as much as 0.1 nm, spectral filters must be able to adapt their central wavelength relative to this shift.

The requirements placed on the filter by the Agency are very demanding. The filter (or combination thereof) is to possess a bandwidth of 0.17 nm and transmission of 90% at the wavelength of 1550 nm. Multiple technologies available for narrow-band spectral filtering have been evaluated in the project: narrow-band interference filters, Fabry-Pérot etalons (FPE), volume diffraction gratings, single- or multi-fiber Bragg gratings, multiple fiber Bragg gratings, multiple cavity gratings, combinations of FPEs or volume Bragg gratings (VBG) with a long wave blocking filters, and a combination of an FPE with a VBG.

This broad analysis has led to the choice of two most promising cascaded filters: FPE with a bandpass filter (BPF) or FPE with a reflecting VBG. Subsequent simulations of the expected performance of either of these combinations have been performed under emulated atmospheric turbulence. The parameters used for the simulations of the filter models match values that are realistically used in such filters. High angular magnification due to the ratio between the aperture D of the telescope and the aperture size of the filter, as well as physical optical propagation to model diffraction efficiency of the filters were used.

2.1 Fabry-Pérot etalon

The FPE is a form of thin-film interference filter where the coating layers are symmetric about a central cavity. Combinations of high- and low-index coatings are used to induce multiple beam interference. Light reflected from the filter interfaces undergoes zero- and 180-degree phase shifts. A double pass through each layer introduces an additional path difference of half the wavelength, such that all reflected light is in-phase yielding constructive interference[3].

FPEs produce periodic transmission comb functions that are separated by the free spectral range (FSR). The full-width at half maximum (FWHM) of the transmission peaks and the FSR are the most relevant characteristics of the FPE. They can be tuned through selection of the materials used to create the cavity, substrate thickness and reflectivity. To comply with the FWHM of 0.17 nm and the central wavelength $\lambda_0 = 1550$ nm, the appropriate cavity design is a fused silica with refractive index $n_0 = 1.444$ and cavity thickness of 117.51 μm. These parameters result in an analytical FSR of 10.27 nm with an FWHM of 0.17 nm. The spectral response of this FPE design is shown in Figure 1.
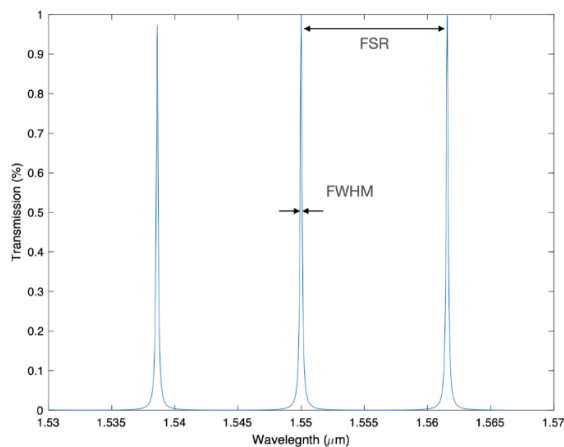
Figure 1. Free spectral range and full width at half maximum of FPE.

For a beam with a flat wavefront that is incident perpendicular to the FPE, the transmission is high, and has values greater than 0.9 for each wavelength sampled over the laser line width. However, a wavefront deformed by atmospheric turbulence can be treated as hitting the FPE under varying local tilts. The stronger the turbulence is, the greater are the local tilts. To account for these, transmission maps for each sampled wavelength are determined and averaged to yield a transmission map for each turbulence scenario analyzed in this project. These scenarios considered: three aperture diameters of the optical ground station ($D = 1$, 4, and 6 m) and two wavefront coherence lengths ($r_0 = 10$ and 20 cm). This yielded 6 different turbulence scenarios specified by the normalized turbulence strength D/r_0 ranging from 5 to 60. Phase screens have been generated for each such scenario according to the prescription described in Ref. 2.

A variation in filter transmission across a phase screen is due to the variation in the local incident angle. The mean efficiency (η_{mean}) of the filter is determined from:

$$\eta_{mean} = \frac{\sum_N \eta(\lambda)}{N} \tag{1}$$

where $\eta(\lambda)$ is the wavelength specific efficiency and N is the number of singular wavelengths sampled over the laser line width. The mean transmission for each turbulence scenario is given in Table 1. The FPE is shown to exhibit high transmission, even in the presence of turbulence.

Table 1. Parameters used in the analytical SHS simulations.

D/r_0	Telescope Diameter [m]	Mean Transmission	Peak Wavelength Shift [nm]
5	1	0.948	1549.981
10	1	0.948	1549.981
20	4	0.936	1549.977
30	6	0.934	1549.977
40	4	0.935	1549.975
60	6	0.930	1549.976

To account for the Doppler shift in the communications signal, the peak transmission wavelength of the FPE has to be tuned. This can be done by heating or cooling the FPE: thermal expansion of the fused silica substrate changes the resonant frequency of the optical cavity formed between the reflective surfaces of the filter[4]. An oven around the FPE has therefore been designed by mBryonics. This oven can precisely tune the filter's central wavelength following a demonstrated linear behavior (see Figure 2). This simulated device uses a thermoelectric cooler, an insulating shell and a ring heater to thermally tune the FPE.
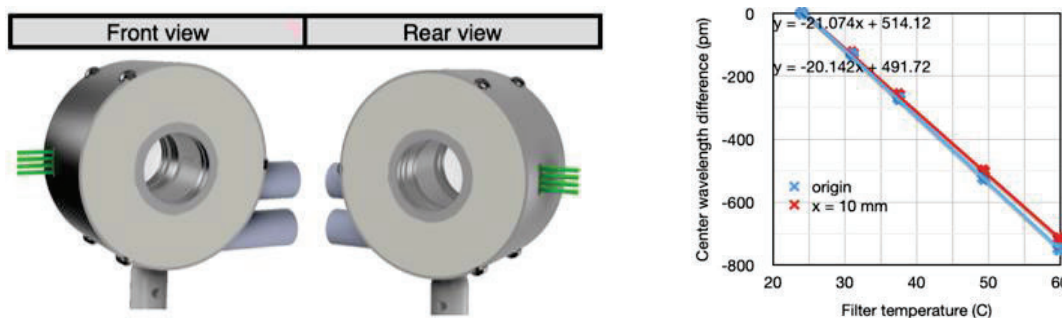
Figure 2. Left: a 3D representation of the proposed device for actively heating and cooling the FPE. Right: a plot of the central wavelength shift from 1550 nm against FPE temperature.

2.2 Reflective volume Bragg grating

Reflective Bragg gratings are spectrally selective elements with a high diffraction efficiency and a characteristic rectangular spectral profile. This spectral profile ensures uniform laser line width transmission at the peak of filter transmission and extends to the limits of the filter's FWHM. Spectral tuning of a VBG is generally carried out by tilting

the filter. Due to the narrow bandwidth of the filter, the filter is sensitive to the local slopes of the wavefront typically induced by turbulence.

The diffraction efficiency of a reflecting VBG asymptotically approaches 1 with an increase in grating thickness or an increase in refractive index modulation[5]. VBG parameters will influence the reflected spectrum. These parameters are substrate thickness, index modulation, and position and size of the probe beam. During simulations, the thickness of the photo-thermo-refractive material is set to 11 mm, the average refractive index of the substrate is set to $n_0 = 1.444$, the modulation of the index has a value of 1.2×10^{-4} and the filter is oriented 6.625° relative to the optical axis. The spectral response of a VBG using those parameters is shown in Figure 3.
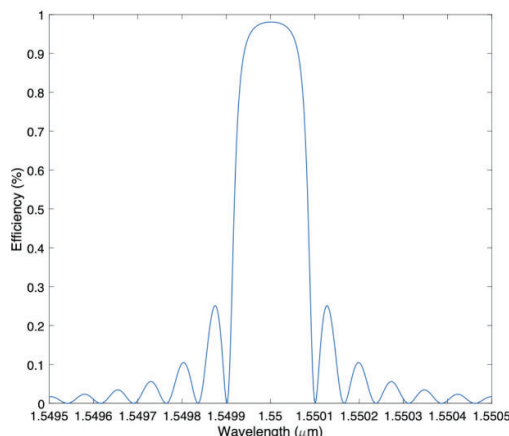
Figure 3. Diffraction efficiency as a function of wavelength for the reflecting VBG.

Wavefront aberrations give rise to a reduction in diffraction efficiency of the reflecting VBG. This does not arise from a global residual tilt, but from local perturbations in the wavefront yielding a shift of the resonant wavelength peak. By tilting the VBG by an angle corresponding to the root mean square (RMS) wavefront slopes, the central wavelength peak is shifted back to 1550 nm. The RMS slopes in question are the magnified slopes at filter interface, which can be used to check the agreement between the statement and corrective tilt.

Table 2 shows the efficiency of the VBG for sample phase screens. The diffraction efficiency (DE) of the filter decreases with increasing values of D/r_0 yielding a larger resonant wavelength shift. The columns labelled "Before Correction" refer to the VBG at its nominal angular position. The RMS slopes for each phase screen are calculated and the angle used to tilt the VBG from its nominal position is used to compensate for the spectral shift. The diffraction efficiency after correction is the performance of the filter after it has been tilted and the peak wavelength corresponds to the resonant wavelength.

Table 2. Diffraction efficiencies (DE) of VBG before and after compensation for six turbulence levels.

D/r_0	Telescope Diameter [m]	DE Before Correction	Peak Wavelength Before Correction [nm]	RMS Slope [deg]	DE After Correction	Peak Wavelength After Correction [nm]
5	1	0.947	1549.952	0.0207	0.978	1549.982
10	1	0.962	1549.995	0.0330	0.980	1550.009
20	4	0.178	1549.859	0.0703	0.970	1549.967
30	4	0.053	1550.153	0.0954	0.980	1550.012
40	6	0.233	1549.877	0.0918	0.978	1550.018
60	6	0.169	1550.297	0.1939	0.980	1550.009

Even though the projected performances of the VBG and FPE are comparable in the absence of turbulence, as can be seen in Table 2, the VBG would not be recommended as a suitable filter for telescopes with diameters exceeding 1 m and with D/r_0 values greater than 10 (on large telescopes) due to its the sensitivity to wavefront perturbations. Application of the

VBG in conjunction with AO would imply real-time tilting of the former in response to AO closing the loop and suppressing local wavefront tilts. On the other hand, it is not certain that AO would work at all if the VBG placed upstream from AO delivers poor performance (which decreases SBR "seen" by AO). For this reason, a combination of an FPE and a bandpass filter (BPF) with 10 nm bandwidth was implemented in the demonstrator.

2.3 Bandpass filter

The function of the BPF is to block out unwanted transmission combs produced by the FPE and to increase the out-of-band rejection by additional orders of magnitude. To be of maximum benefit, the bandpass filter is recommended to be positioned before the FPE. With this arrangement the wavefront sensor benefits from both spectral filters.

The optical density (OD) of a BPF, an FPE as well as the combination of both is shown in Figure 4. For BPF specification we have selected the commercially available filter NIR01-1550/3-25 from Semrock. FWHM is specified as approximately 8.8 nm and the transmission at 1550 nm as >90%. The FPE was designed with the optimized set of parameters discussed in Section 2.1 having an FWHM of 0.17 nm. The OD is shown for the spectral region of 1-1.7 μm. In an operational system, shorter wavelengths will be most likely cut out by a window in front of the communications detector and longer wavelengths may be cut out by an optional additional long-wave blocking filter[6].
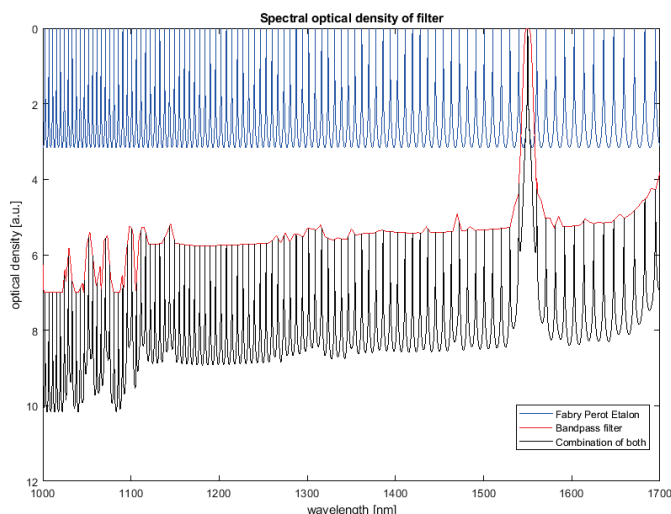
Figure 4. Simulations of optical density of cascaded filter with FPE (blue), BPF (red), and the combination of both (black).

We have compared the out-of-band transmission of this filter combination with the transmission of a perfect rectangle filter with a transmission bandwidth of 0.17 nm. We found that the transmission of the combination of a commercial-off-the-shelf (COTS) BPF and FPE would incur a penalty of only ~1.5 in increased background transmission.

2.4 Characterization of the filters

The COTS BPF filter "HC Laser Clean-up NIR 1550/3" from AHF Analysentechnik has been ordered for inclusion in the demonstrator. According to specifications, it provides 8.8 nm FWHM as well as a transmission coefficient above 90% at 1550 nm. A custom FPE was designed and manufactured by SLS Optics to provide an FWHM of 0.17 nm with an FSR of 9.88 nm. Independent characterizations of both devices had to be done outside of the demonstrator as the free-space background generator cannot be used for fiber coupling which is mandatory for optical spectrum analysis.

The 10-nm BPF has been characterized with the use of a spectrometer UV-3600 from Shimadzu. The measured FWHM was 8.5 nm which fits the specification (8.8 nm) and should properly cut the secondary peaks of the FPE. A noticeable shift in the pass band has been measured, as it is centered at 1552.5 nm rather than the expected 1550 nm. This however can be easily corrected by tilting the filter when positioned in the demonstrator, because introducing an angle in the incident beam relatively to the surface of the BPF will shift the pass band towards lower wavelengths, compensating for this 2.5 nm off-centering. Table 3 summarizes the results of characterization.

Table 3. Verification of the most relevant specifications of the BPF.

Parameter	Data sheet	Measured	Unit
Central wavelength	1550 ±3	1552.5	nm
FWHM	8.8	8.5	nm
Transmission between 1548.5 and 1551.5 nm	> 90%	> 90%	-

The FPE allows for very fine spectral filtering of light, but has to be used in conjunction with the BPF, as its transmission peaks occur periodically over the optical spectrum. The FSR that defines this periodicity was required to be 9.88 nm so that the secondary transmission peaks are cut by the 10-nm BPF. The FWHM was also designed to be between 0.18 nm and 0.23 nm to produce very fine spectral filtering. The optical spectrum analyzer (OSA) used for the characterization of the FPE has a narrow bandwidth of 39 nm, but a very fine resolution of 2.5 pm. This bandwidth is sufficient to measure at least 3 transmission peaks, as they are expected to be separated by an FSR of ~10 nm, and the resolution is two orders of magnitude finer than the expected FWHM of the transmission peaks. From the OSA measurements an FWHM of 0.227 nm and an FSR of 9.95 nm have been found, which is commensurate with the specifications delivered by SLS Optics.

The wavelengths filtered by the FPE depend on the angle of incidence of the light. For this reason, the FPE has been mounted in a piezo mount 8822-AC from Newport that offers an angular resolution of 0.7 µrad. A minimum angular resolution of 64 µrad is necessary to achieve accurate positioning of the FPE in order to filter a specific wavelength. With the motorized mount, 150 measurements of the transmission spectrum, each separated by a known angle, have been performed to verify the reproducibility and reliability of the FWHM and FSR. Through all measurements performed, the two parameters have matched the specifications given by the manufacturer as summarized in Table 4.

Table 4. Verification of the most relevant specifications of the FPE.

Parameter	Data sheet	Measured	Unit
FSR	9.88	9.95	nm
FWHM	0.224	0.227	nm
Peak transmission	83.6 %	86 %	-

3.   BREAD-BOARD DEMONSTRATOR

Following the simulations[2] and the characterization of transmission filters described in Section 2, a laboratory demonstrator of spectral and spatial filtering for low-SBR, low-photon-count applications has been set up. Due to financial constraints, photon-counting detectors have not been included in the system. It has been instead decided to construct a demonstrator based on COTS technologies.

Three SBR scenarios have been emulated (SBR = 1, 0.05 and 0.02). Here SBR is defined as ratio of the summed fluxes of the signal and the underlying background within an area encircling 80% of the total photon flux on the communications detector in seeing-limited operation (no AO but presence of a spectral filtering subsystem with a bandwidth of 0.17 nm). We note that for each SBR scenario absolute photon fluxes have been varied to accurately produce the desired SBR:

Figure 5 shows a photograph and a schematic of the demonstrator. The most important components are: two X15213-08 SLMs from Hamamatsu, Goldeye G-033 TEC1 infrared camera from Allied Vision, HASO SWIR Shack-Hartmann sensor from Imagine Optic, and the two transmission filters discussed in Section 2. To generate background light that reaches the detector as well as the wavefront sensor plane, we have designed and built a background generator. As a light source we used a halogen lamp (HALOSTAR PRO 50 W 12 V GY6.35) from Osram. To simulate background light entering the optical system, we used a transmitting quartz diffuser "Diffusil" because it is designed to create an almost perfect Lambertian light output over a wide wavelength range. The plane of the diffuser is imaged onto the detector and the wavefront sensor plane. With this, we ensure that the background detected by the SHS is omnidirectional. Even though the background generator has demonstrated good illumination homogeneity, digitally adding background light to the images acquired by the detector of the SHS provided much higher flexibility and precision when evaluating the system.

The two SLMs, which are positioned in conjugate pupil planes, are used to emulate and correct turbulence respectively. A deformable mirror has been deliberately omitted from the demonstrator in order to show whether AO can provide *any* meaningful improvements at an SBR ~1 and with very few photons.
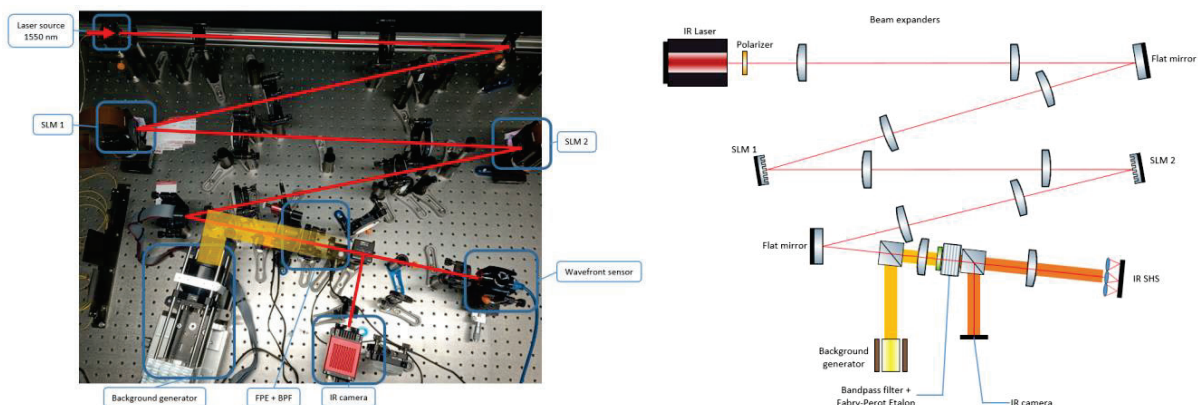
Figure 5. Left: photograph of the bread-board demonstrator. Right: its schematic design.

Significant effort has been invested in designing new centroiding algorithms capable of extracting SHS spot displacements for situations where the noise levels are of the same magnitude as the signal. A modal wavefront reconstructor has also been implemented, and its parameters were tuned for each SBR and D/r_0. Two AO controllers have been tested, namely: a pure integrator and a leaky integrator. These investigations are described in the companion paper[2].

Tip and tilt (TT) correction was not the focus of this study and therefore all turbulent phase screens had their average slope removed before displaying them on the SLM. In the end, improvements due to high-order AO have been obtained for many scenarios, but only for SBR = 1 and not for SBR = 0.05 or 0.02. Figures 6 and 7 show example point-spread functions (PSFs) with TT-only correction and with high-order AO, for D/r_0 = 5 to 20. Quantitative results in terms of the Strehl ratio are listed in Table 5. It should be noted that improvements in the Strehl ratio of the long-exposure PSF for SBRs down to 0.2 have been achieved.
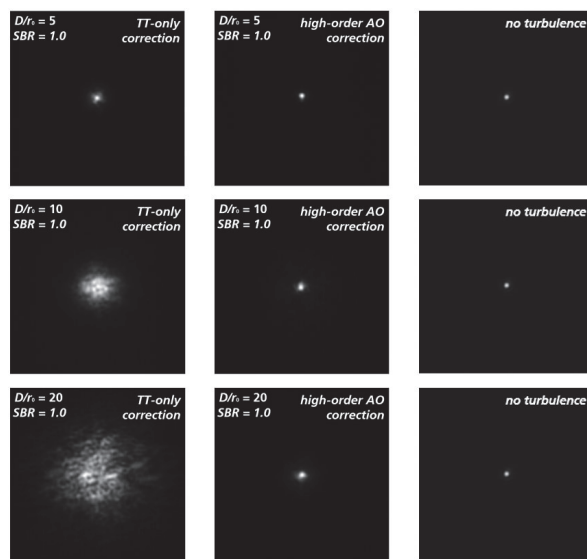
Figure 6. Example results obtained with the demonstrator. The panels show average PSFs imaged on the SWIR camera, when the SLM displayed input phase screens with tip and tilt subtracted digitally (left), when AO was switched on (center), and when the SLM was set to a flat position.
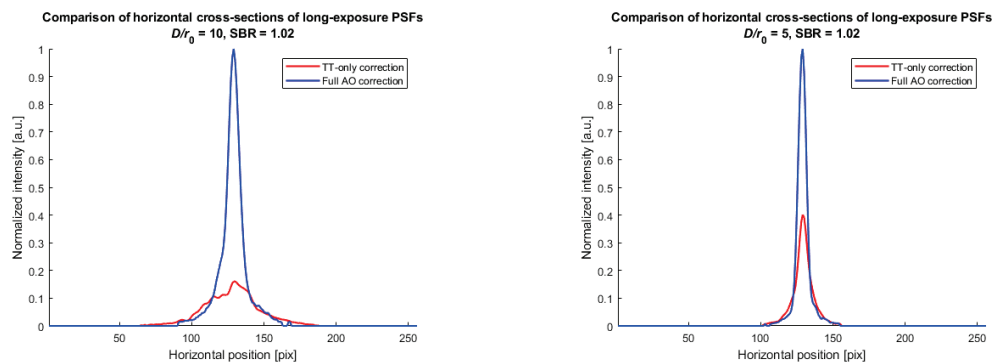
Figure 7. Comparison of the cross-sections of the PSFs, scaled by the peak of the PSF with the higher Strehl ratio, with perfect TT correction (in red) and with full AO correction (in blue) under SBR = 1. Left: for $D/r_0 = 10$. Right: for $D/r_0 = 5$.

Table 5. Comparison between the results obtained from simulations[2] and from the bread-board demonstrator. Improvement factors are given in terms of the Strehl ratio (SR) enhancement with respect to the PSF generated with perfect TT correction for the three SBR values of 1, 0.05 and 0.02. The cases where AO has brought no improvement or even deterioration are not shown.

D/r_0	SBR	SR with perfect TT correction	Simulations		SR with perfect TT correction	Demonstrator	
			SR after high-order AO correction	Improvement factor		SR after high-order AO correction	Improvement factor
5	1		0.4525	2.46		0.4238	2.48
5	0.05	0.1840	-	-	0.1709	-	-
5	0.02		-	-		-	-
10	1		0.2183	8.01		0.1425	7.09
10	0.05	0.0273	-	-	0.0201	-	-
10	0.02		0.0620	2.28		-	-
20	1		0.3108	39.42		0.1664	33.28
20	0.05	0.0079	-	-	0.0050	-	-
20	0.02		-	-		-	-

For SBR = 1, the demonstrator yielded improvement factors of a magnitude comparable to the results obtained through simulations[2] of SHS-based AO correction. Improvements ranged from 2.5 to 34 with respect to tip/tilt-only correction. No increase in SR has been obtained for SBR = 0.05 or 0.02. Because higher SRs translate to a narrower focal-plane spot on the detector, these results are promising and show that daytime AO using tens of signal photons for wavefront sensing could allow for much smaller detectors to be used for deep-space communications than currently assumed.

4.   ROADMAP TOWARDS AN OPERATIONAL SYSTEM

The applicability of the final results and of the background rejection system created in the laboratory to a fully operational system has been evaluated. The real-world system requires operation in a photon-counting regime; a cryogenic cooling module is therefore required to make full use of a photon-counting SWIR detector in the operational SHS[7]. To avoid a strong temperature gradient in the SHS that could result in damage-inducing mechanical constraints, it is thus advised to encase the microlens array, detector, and any field-stop in a cryogenic module. The SHS should be cooled down to ~80 K during operation but stored at room temperature (~290 K) otherwise. As the microlens array will be glued onto the outer frame of the detector, its mechanical and material specifications have to be considered to avoid a strong thermal expansion

coefficient. Each lenslet should be designed to cover a 5x5 pixel area (3x3 region of interest (ROI) with one line of guard pixels between each ROI) on the chosen SWIR camera to be used as the SHS detector.

The breadboard demonstrator only accounts for correction of high-order aberrations as tip and tilt are typically pre-corrected with the use of a separate fast steering mirror to avoid saturation of the deformable mirror's (DM) stroke. COTS fast steering mirrors designed for TT correction will have to be included in the AO system of the optical ground station.

The following three parameters are the most important ones when choosing an appropriate DM: actuator stroke, number of actuators, and update rate. The emulated scenarios pose no challenges in terms of either the actuator density or the bandwidth of the DM. In terms of stroke, a DM able to cover even the most extreme case of $D/r_0 = 60$ would require 32 actuators across the mirror diameter and a peak-to-valley mechanical stroke of 7 µm. Such mirrors are available on the market and Figure 8 shows that the required DM stroke can be fulfilled by two example devices up to $D = 4$ m (for $r_0 = 10$ cm) and up to $D = 8$ m (for $r_0 = 20$ cm).
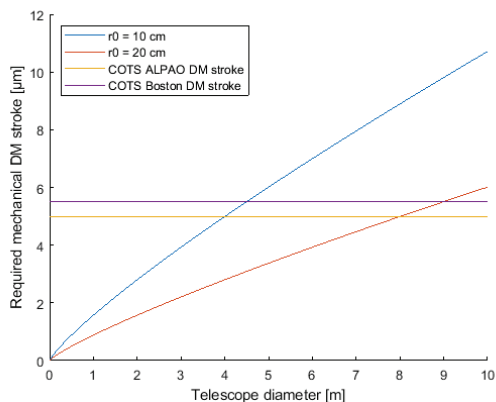
Figure 8. Required peak-to-valley stroke of a DM as a function of the telescope diameter for two different r_0 values (at 1550 nm). Horizontal lines represent the maximum strokes of two commercially-available DMs.

The question of the benefits of using a laser guide star (LGS) as opposed to a natural guide star (NGS) mode, which is implicitly used in this project, has been also addressed. As the performance of any AO system is dependent on the number of photons it receives, the use of an LGS could in principle reduce the measurement error stemming from photon-counting operation. LGS are based on either Rayleigh scattering of the atmosphere or excitation of the mesospheric layer of sodium. As the second method samples a larger portion of the atmosphere (laser guide focused at ~15 km for Rayleigh scattering compared to ~90 km for sodium layer excitation), focal anisoplanatism is reduced. However, as both these technologies do not allow for measurement of tip and tilt, image jitter must be sensed with a separate detector looking at an NGS. Due to the dominant background sky radiation during daytime, observation of an NGS is not possible and TT correction would have to rely on the communications signal at 1550 nm. If a separate TT measurement channel is to be avoided in order to minimize losses to communications, then the detector used for communications must serve also as a position detector. Superconducting Nanowire Single Photon Detectors (SNSPDs) meet this requirement thanks to single photon detection. An SNSPD can be divided into four quadrants for measuring angle of arrival in photon-counting regime[1].

Through the use of an LGS, the SHS would not have to work in a photon-counting regime but would still be flooded by background light during daytime operation. The use of a narrow spectral filter tuned at the wavelength of the LGS (589 nm in the case of the sodium LGS) is still mandatory to perform wavefront sensing. Application of FPEs to isolate the LGS signal from the sky background has not been studied, but good performance of magneto-optical filters for daytime observations with an LGS has been demonstrated[8].

On the other hand, opting for an LGS for wavefront correction removes the need for an expensive and fast, sub-electron SWIR detector used in an SHS sensor. A COTS, electron-multiplying charge-coupled device (EMCCD) can be used as the SHS detector when measuring the wavefront from an LGS[9]. A scientific-grade, complementary metal-oxide-semiconductor (CMOS) detector can be used as the SHS detector if it can receive 20 photons per pixel per exposure[10]. Both the EMCCD and CMOS detectors operate at a framerate high enough to not limit the performance of the AO control loop.

An LGS created by Rayleigh scattering of an ultraviolet source offers a cheaper alternative to a sodium LGS to the detriment of a higher focal anisoplanatism. An alternative to LGS AO is to rely entirely on the sub-electron noise SWIR detector for sensing both, TT and higher-order aberrations in a pure NGS configuration. In this strategy, the SNSPD is used exclusively for communications.

5. SUMMARY

During the project, a spectral and spatial filtering system has been designed, optimized and prototyped in the laboratories of Fraunhofer IOSB. Firstly, through preliminary studies, the most promising technologies for spectral and spatial filtering have been identified. After performing simulations for a broad parameter space for each type of filter, it was decided that the laboratory demonstrator should be based on a Fabry-Pérot etalon coupled with a bandpass filter and a Shack-Hartmann wavefront sensor. A breadboard demonstrator has been implemented to validate the performances of the proposed technologies.

The demonstrator has yielded improvements in the Strehl ratio in the range of 2.5 to 34 with respect to tip/tilt-only correction. These results, obtained for SBR = 1, denote a significant improvement factor for the Strehl ratio considering the amount of noise and signal on the detector are equal in such a scenario. The custom centroiding algorithm used for wavefront reconstruction demonstrated good performance, whereas the classic centroid measurement approach failed. Proper optimization of the trade-off between the number of Shack-Hartmann lenslets and the number of photons collected by each lenslet was also key.

It should also be noted that we have obtained better relative improvements in Strehl ratio for larger telescopes and higher D/r_0 values for a fixed SBR scenario. Potential real-world implementations of the results obtained in the demonstrator would require the use of photon-counting devices. Available technologies to reach the ultimate performance of the future operational system have been identified. Possible future development of a full-scale AO system for deep-space optical communications following the same conceptual architecture as the prototype presents no technological bottleneck.

ACKNOWLEDGMENTS

REFERENCES

[1] L. C. Roberts Jr, S. Meeker, S. Piazzola, J. C. Shelton, "Daytime adaptive optics for deep space optical communication," Proc. SPIE 11133, 1113308, (2019).
[2] S. Gladysz, A. Zepp, R. Bellossi, M. Segel, D. McDonald, K. Stein, "Adaptive optics for daytime deep-space optical communications," Proc. SPIE 12237, (2022).
[3] H. A. MacLeod, Thin-film optical filters. CRC Press, (2017).
[4] K. Shtyrkova, I. Gaschits, and D. O. Caplan, "Narrowband optical filtering for background-limited photon-counting free-space optical communications," Proc. SPIE. 10910, (2019).
[5] I. V. Ciapurin, V. Smirnov, D. R. Drachenberg, G. B. Venus, and L. B. Glebov "Modeling of phase volume diffractive gratings, part 2: reflecting sinusoidal uniform gratings, Bragg mirrors," Optical Engineering 51, 058001 (2012).
[6] Y. Chen and H. Hemmati, "Optical filter assembly for interplanetary optical communications," Proc. SPIE 8610, 86100R, (2013).
[7] T. Greffe, P. Feautrier, J.-L. Gach, E. Stadler, F. Clop, S. Lemarchand, D. Boutolleau, and I. Baker "C-RED One: the infrared camera using the Saphira e-APD detector", Proc. SPIE 9907, 99072E (2016).
[8] M. Hart, S. Jefferies, and N. Murphy, "Daylight operation of a sodium laser guide star," Proc. SPIE 9909, 99095N (2016).
[9] J. Aceituno, S. F. Sanchez, J. L. Ortiz, and F. J. Aceituno "SAOLIM, Prototype of a Low-Cost System for Adaptive Optics with Lucky Imaging. Design and Performance," Publications of the Astronomical Society of the Pacific, 122, (2010).
[10] Andor Technology Ltd, private communication